

# Analysis of Left Ventricular Wall Motion Based on Volumetric Deformable Models and MRI-SPAMM\*

Jinah Park<sup>1</sup>, Dimitri Metaxas<sup>1</sup> and Leon Axel<sup>2</sup>

<sup>1</sup>Department of Computer & Information Science  
University of Pennsylvania  
Philadelphia, PA 19104-6389, USA  
jinah@graphics.cis.upenn.edu  
dnm@central.cis.upenn.edu

<sup>2</sup>Department of Radiology  
University of Pennsylvania  
Philadelphia, PA 19104-6086, USA  
axel@spammgw.mipg.upenn.edu

## Abstract

We present a new approach for the analysis of the left ventricular shape and motion that is based on the development of a new class of volumetric deformable models. We estimate the deformation and complex motion of the left ventricle (LV) in terms of a few parameters that are functions and whose values vary locally across the LV. These parameters capture the radial and longitudinal contraction, the axial twisting, and the long-axis deformation. Using Lagrangian dynamics and the finite element theory, we convert these volumetric primitives into dynamic models that deform due to forces exerted by the datapoints. We present experiments where we used magnetic tagging (MRI-SPAMM) to acquire datapoints from the LV during systole. By applying our method to MRI-SPAMM datapoints, we were able to characterize both locally and globally the 3D shape and motion of the LV in a clinically useful way. In addition, based on the model parameters we were able to extract quantitative differences between normal and abnormal hearts and visualize them in a way that is useful to physicians.

**Keywords:** Physics-based modeling, Volumetric deformable models, Left ventricle (LV), Intuitive parameters, Quantitative shape and motion analysis.

## 1 Introduction

Estimating the volumetric shape, motion and deformations of the left ventricle (LV) accurately, and in a clinically useful way, is a very important yet open research problem. Conventional cardiac imaging methods (e.g., MRI) still have many limitations, such as no explicit data correspondence between frames, and insufficient resolution of the extracted data. In addition, most of

the existing models for the analysis of the LV shape and motion are based on the use of parameters that are either too complex or too few to be used by a physician.

Recently, a new magnetic resonance imaging (MRI) technique based on *magnetic tagging* (MRI-SPAMM) has been developed at the University of Pennsylvania for imaging of regional heart wall motion (Axel and Dougherty, 1989). This fast, non-invasive technique promises to be very useful in the analysis of heart wall motion because it provides temporal correspondence of material points within the heart wall. This correspondence, in conjunction with the use of the three-dimensional (3D) location of each tagged datum, can subsequently be used as input to a motion analysis technique to extract the three dimensional left ventricular motion parameters. The motion parameters can then be statistically analyzed to explore their correlation with the various types of LV disease.

While there is some initial experience in the use of tagged MRI and related techniques to study the 3D motion of the heart, there is still no generally accepted method for analysis and display of the 3D heart motion. For example, Young and Axel (1992) previously developed a finite element based method for reconstructing the 3D motion and deformation of the LV from MRI-SPAMM data. Although their method has provided a good local strain analysis, their model results in a large number of model parameters which must be non-trivially post-processed to provide meaningful geometric information on the nature of the deformation.

In an effort to overcome the limited clinical usefulness of most existing models for analyzing the LV, we have previously developed a new class of deformable 3D *surface* models whose deformations can be described with a small number of intuitive parameters that are functions (Park *et al.*, 1994, 1996). These parameter functions comprise an *intelligent* grouping into a small

---

\*US patent pending

number of sets, of the many local parameters that are necessary to analyze the LV mid-wall. An example of a parameter function is longitudinal contraction, which is the set of parameters describing the contraction of the LV from the apex to the base. Based on this new model, we can analyze both locally and globally the shape and motion of the LV in a way that is readily understood by a physician.

In this paper, we first extend the above class of deformable **surface** models to develop a new class of **volumetric** deformable models that can analyze in a clinically useful way the volumetric motion of the LV. Second, we develop a new quantitative algorithm for the calculation of forces exerted from MRI-SPAMM data to our deformable model. The force calculation algorithm is based on the constrained physical motion of SPAMM datapoints in three dimensions. We combine forces from SPAMM datapoints originating at two sets of orthogonal planes, since only the in-plane motion of a SPAMM datapoint from a given set of planes can be estimated. In addition to forces from the SPAMM datapoints, we use forces from datapoints sampled from the inner and outer walls of the LV to estimate its shape. The combination of forces from boundary and SPAMM datapoints allows the extraction of the volumetric shape and motion of the LV. We also develop a new set of visualization tools which include parameter graphs, a 3D representation of the LV shape and motion, and the color-based mapping of the model's parameters on the 3D volumetric model. These tools allow the quantitative analysis of the LV shape and motion, and the visual representation of the analysis results in a clinically useful manner. Finally, based on the above new model we were able to quantitatively verify and visualize in 3D the knowledge about the LV that was qualitatively known to physicians.

The rest of this paper is organized as follows. Section 2 gives a summary of previous work. Section 3 describes the various types of imaging modalities used to provide data for the LV analysis. Section 4 formulates the geometry of the new class of volumetric deformable models. Section 5 presents the new algorithm for computing forces from the SPAMM datapoints to the deformable model. Section 6 gives a detailed analysis of the model parameters used in our model. Section 7 describes the model fitting procedure to the SPAMM datapoints. Section 8 presents the experimental results of our model. Finally, Section 9 gives the conclusions.

## 2 Related Work

There have been many model-based approaches to the analysis of the complicated motion of the LV, and the quantification of its measured deformation. Simple an-

alytical models like spheres, ellipsoids or cylinders are often used. For example, Beyar and Sideman (1985) constructed a mechanical model where the LV is modeled as a nested shell spheroidal to explain the effect of twisting motion; Arts *et al.* (1982) used a thick-walled cylinder composed of eight concentric cylinder shells to describe the LV deformation; Kim *et al.* (1985) used a thick-walled ellipsoidal model for the computation of the LV wall stress, and a truncated ellipsoidal model for simulation of regional stress; Azhari *et al.* (1992) used a hollow conical shell (with a constant shear modulus) to characterize transmural twist motion; and Arts *et al.* (1992, 1993) developed a kinematic model by combining the deformation modes from a spherical, a prolate ellipsoidal and a cylindrical model.

However, the shape of the LV is neither spherical nor cylindrical. Even a prolate ellipsoid is a gross simplification of the shape of an LV. Therefore, as Guccione and McCulloch (1991) pointed out, the analyses made by these models make simplifying assumptions about the material behavior of the heart muscle and the governing equations of motion.

Recently, techniques based on the use of deformable models for reconstructing the 3D *surface* shape and motion of the LV from CT or MRI data have been developed (e.g., Amini and Duncan, 1991; Cohen and Cohen, 1990; Huang and Goldgof, 1993; McInerney and Terzopoulos, 1993; Nastar and Ayache, 1994; Shi *et al.*, 1994). They use finite elements, spring-mass systems, deformation modes, bending and stretching thin-plate models, and other physics-based or geometric techniques. The main limitation of these techniques is that they do not provide intuitive motion parameters to model the rigid and non-rigid motion of the LV. Most of the techniques represent the LV motion as a set of local displacement vectors which either requires non-trivial post-processing to be useful to a physician or is only good for qualitative visualization (Amini and Duncan, 1991; Chen and Huang, 1990; Cohen and Cohen, 1990; Huang and Goldgof, 1993; McInerney and Terzopoulos 1993; Mishra and Goldgof, 1991; Shi *et al.*, 1994). On the other hand, models developed by Bardin *et al.* (1994) or Friboulet *et al.* (1992) are formulated in terms of very few parameters that can offer only a gross approximation to the motion of the LV. And attempts to characterize the LV motion based on deformation modes do not provide a localization of the LV deformations and motion in a clinically useful manner, due to the global definition of each modal deformation (Nastar and Ayache, 1994; Pentland *et al.*, 1991). Moreover, most techniques ignore the twisting or wringing motion of the LV known to occur during systole. To overcome the above limitations, we have previously developed a new class of surface deformable

primitives whose global parameters are functions, and have demonstrated that the LV surface shape and motion can be accurately represented with these parameters that can be easily interpreted by physicians (Park *et al.*, 1994). The input to these models were datapoints sampled from the mid-wall surface of the 3D finite element model of Young and Axel (1992).

However, the LV motion cannot be captured entirely with surface models. To capture the LV shape and motion throughout its volume, we need a *volumetric* deformable model. Recently, techniques for analyzing the volumetric LV shape and motion from tagged MR image sequences have also been developed based on the use of 3D finite elements (Denney and Prince, 1994; Moore *et al.*, 1992; O’Dell *et al.*, 1993; Young and Axel, 1992). Such model-based approaches to the recovery of the volumetric shape and motion of the LV are necessary in order to overcome the limitation of current medical imaging modalities. Such modalities cannot provide explicitly, the time-varying 3D motion of material datapoints from the LV. The translation of the deforming heart through the fixed image planes puts a different cross section of myocardium into the image plane at each time point. Therefore the imaging techniques can provide only the two-dimensional motion of material points on the imaging plane at best.

Finite element modeling is a typical choice for volumetric motion analysis, since it provides strain analysis throughout the ventricular wall. However, the finite element representation does not directly lend itself to an understanding of the underlying kinematics in a clinically useful way. The parameters of the model are nodal displacements, resulting in a relatively large number of parameters, the physical interpretation of which can be difficult. The 3D strain tensor, for example, has three normal components and three shear components, each of which may vary with position in the wall. In order to understand the complex relationship between these components and other motion parameters, it is desirable to characterize the motion in terms of meaningful physical parameters that offer sufficient accuracy. In the remaining sections, we will demonstrate how this can be achieved with our technique.

### 3 Data Extraction Techniques for Cardiac Motion Studies

Characterization of heart wall motion on a regional level is required to understand cardiac mechanics and the processes underlying a disease. In order to accurately measure heart wall motion, a number of material points must be located and tracked. Methods for providing intra-myocardial markers in the past have included the

implantation of radiopaque markers (Arts *et al.*, 1993; Brower *et al.*, 1978; Harrison *et al.*, 1963; Meier *et al.*, 1980), lead beads (Waldman *et al.*, 1985), or ultrasonic crystals (Rankin *et al.*, 1976; Villarreal *et al.*, 1988), use of naturally occurring landmarks (Chen and Huang, 1990; Kim *et al.*, 1985; Young, 1991; Young *et al.*, 1992), and magnetic resonance (MR) tagging (Axel and Dougherty 1989; Azhari *et al.*, 1992; Denney and Prince, 1994; Fischer *et al.*, 1994; Moore *et al.*, 1992; Zerhouni *et al.*, 1988).

Although the implantation methods have been used for the LV motion analysis, and provide accurate localization, the invasive nature of the procedures does not allow a sufficient number of markers to be implanted for describing the LV geometry. Moreover, it poses the potential problem of local myocardium property alteration due to the introduction of foreign objects. On the other hand, the methods which utilize naturally occurring landmarks, like bifurcations of coronary arteries, do not require a surgery and can provide potentially many markers. However, intra-coronary injection of contrast medium is usually required to highlight the blood vessels in acquired images. When the blood supply is severely obstructed due to arterial occlusion, the tracing of the feature points around the region can be very difficult to achieve (Kim *et al.*, 1985).

MR tagging has its advantages over the aforementioned approaches because a large number of material points may be marked and tracked during systole in a non-invasive manner. By locally perturbing the magnetization in tissue, one can create spatially encoded patterns such as star-bursts (e.g., Azhari *et al.*, 1992; Denny and Prince, 1994; Moore *et al.*, 1992; Zerhouni *et al.*, 1988) or grids (e.g., Axel and Dougherty, 1989; Fischer *et al.*, 1994; Young and Axel, 1992). Those patterns or magnetization tags are seen as dark regions in subsequent images (within a certain relaxation time  $T_1$ ). As magnetization moves with tissue, the magnetization tags will move in the corresponding images, directly reflecting the motion of the underlying tissue and allowing us to follow the motion patterns within otherwise featureless structures such as the heart wall. One drawback of current MR tagging techniques, is that the tracking is possible only during systole or diastole at one time (i.e., not for a complete heart cycle), due to the decay of the magnetization signal over time.<sup>1</sup>

#### 3.1 Data Extraction Techniques based on the Derivation of Feature Points

Recently, curvature-based point correspondence recovery techniques have been proposed by researchers as

---

<sup>1</sup>The weakening of the magnetization signal over time can be observed in Fig. 1 as well.

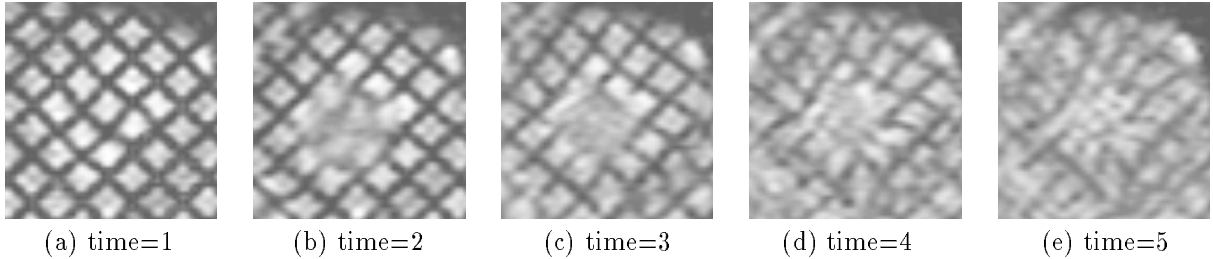


Figure 1: SPAMM images of a left ventricle during systole.

an alternative to the above methods. The method by Goldgof *et al.* is based on the computation of the Gaussian curvature of a model that deforms based on the assumption of conformal motion (Kambhamettu and Goldgof, 1992; Mishra and Goldgof 1991). The method of Amini and Duncan utilizes the potential energy of their bending and stretching model to estimate the curvature (Amini and Duncan, 1991; Shi *et al.*, 1994). Shi *et al.* (1995) combined curvature extraction with Phase Velocity MRI, in an attempt to assess the transmural myocardial deformation in 2D. Friboulet *et al.* (1993) demonstrated the stability of the Gaussian curvature computation in an experiment where the Gaussian curvature was computed through an iterative relaxation scheme from voxel-based surface rendering of CT left-ventricle volumetric data over a cardiac cycle. The derivation of point correspondences based on curvature has a potential in the sense that it can be widely used to datasets from many different medical imaging modalities and it can provide point correspondence over an entire heart cycle. But the technique is still under development.

### 3.2 Data Based on MRI-SPAMM

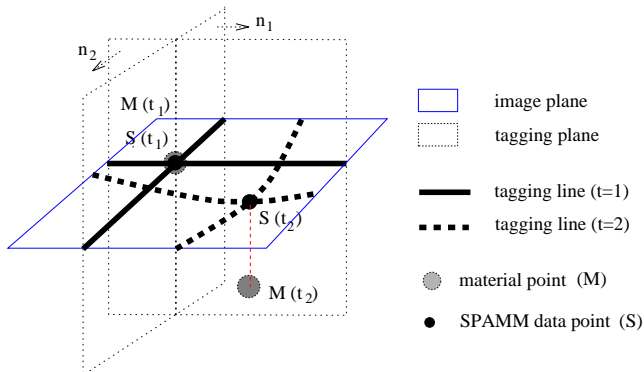


Figure 2: Tagging planes and image planes.

Even though our LV shape and motion estimation technique can be used with any type of LV data, we will apply it to data from MRI-SPAMM (Axel and Dougherty,

1989), an MR tagging method. The advantage of the SPAMM (SPAtial Modulation of Magnetization) technique over the other data extraction techniques, is that a number of material points can be marked in a very short time with a simple procedure, and they can be tracked during systole in a non-invasive setting which provides temporal correspondence of the material points. The SPAMM technique has been previously used to estimate regional motion patterns during systole (Axel and Dougherty, 1989; Rogers *et al.*, 1991; Young *et al.*, 1994), and the methods for estimating material deformation have been validated using deformable phantoms (Young *et al.*, 1993).

The SPAMM data collection technique is based on the application prior to imaging of a saturation pulse sequence where the amplitude of the magnetization varies spatially, in a sinusoidal-like fashion. This saturation pulse sequence forms the *tagging planes* (see Fig. 2). At the minima of this sinusoidal-like variation of the magnetization, dark lines appear in the *image plane* which intersects the tagging planes. If we continue to image the tissue after the saturation pulse sequence is applied, we can see those dark lines move, allowing us to track the motion of the underlying tissue. In order to track points instead of lines, another set of saturation pulse sequences is applied to form a set of tagging planes orthogonal to the previous set of tagging planes. As a result, the grids appear in the image plane. Figs. 1(a-e) show short-axis views of an LV from end-diastole (time=1) to end-systole (time=5), where the SPAMM datapoints are defined by the intersections of the respective dark lines.

Given that every image plane is spatially fixed, while a heart being imaged moves, the through-plane motion (Rogers *et al.*, 1991; Fischer *et al.*, 1994) cannot be captured by the SPAMM datapoints on the image plane. Fig. 2 shows the location of a SPAMM datapoint  $\mathbf{S}$  at two different times  $t_1$  and  $t_2$ . Initially,  $\mathbf{S}(t_1)$  coincides with a material point  $\mathbf{M}(t_1)$ . However, the motion of the SPAMM datapoint between these two time instances corresponds approximately to the components, on the image plane, of the motion of the material point  $\mathbf{M}$  which lies somewhere along the line where the tag-

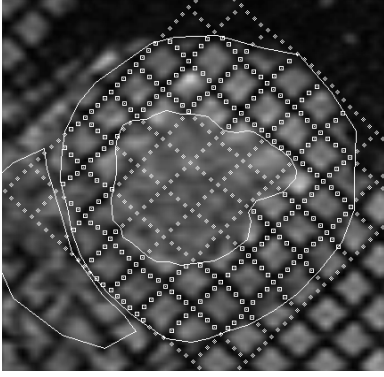


Figure 3: SPAMM datapoint extraction.

ging planes intersect at time  $t_2$  (a possible position of the material point  $\mathbf{M}$  at  $t_2$  is marked in Fig. 2). Therefore, we can obtain only the in-plane motion from MRI-SPAMM images acquired over time. In order to assess the 3D motion of material points of the LV from the set of such 2D time-varying data, we need to combine through a model-based approach, two sets of data obtained from mutually orthogonal image planes.

As described above, each SPAMM datapoint is defined as the intersection of two tagging planes. Young *et al.* (1994) developed a method for extracting the intersection points of tagged lines. The method can be summarized as follows. For each image sequence, the tag stripes within the heart muscle are tracked semi-automatically using a 2D active contour model (Kass *et al.*, 1988). In this procedure, each stripe is discretized into equally spaced points and is modeled as a thin, flexible beam with a small inherent resistance to stretching and bending. Stripes are connected at the intersection points and the entire mesh deforms to track the corresponding intensity values in the image. Fig. 3 shows an instance of tracking the tagging grid and the inner and outer LV walls where active contours are overlaid onto the image. Bilinear interpolation of image intensity between pixels enables sub-pixel resolution in stripe tracking. Only those points between the inner and outer boundaries were influenced by the image, and the remaining inactive points of the grid were maintained to provide a weak continuity for the structure and allow points to move onto/off the image plane.<sup>2</sup>

During the SPAMM acquisition process, the spatial location of each image plane is evaluated based on the acquired spatial locations of the corners of each image plane so that we can express the coordinates of each

<sup>2</sup>This semi-automatic tracking algorithm is incorporated into a software package SPAMMVU (Axel *et al.*, 1993; Young *et al.*, 1995) which is developed at the Radiology Department of the University of Pennsylvania.

datapoint with respect to the centroid of the LV.

It is important to mention that the SPAMM datapoints in the two orthogonal sets of image planes do not correspond to the same material points, but to different material points. These observations will be used in the calculation of the forces exerted from the SPAMM datapoints to the volumetric deformable model.

In addition to the SPAMM datapoints, boundary datapoints from the inner and outer LV walls are also extracted using active contour models and manual initialization. The fully automatic extraction of both the SPAMM and the boundary data is beyond the scope of this paper.

## 4 Volumetric Deformable Models with Parameter Functions

The new class of deformable models we develop in this paper allows the use of global parameters that can characterize a volumetric shape in terms of a small number of parameters that are *functions*. The fact that these parameters are functions and not scalars allows the localization and the detailed estimation of the LV shape and motion. Our technique for creating a primitive with parameter functions to model the LV is based initially on the replacement of the constant parameters of a superellipsoid primitive with differentiable parameter functions (e.g., axial deformation). We then add additional global deformations (e.g., axial twisting) with continuous parameter functions to capture the LV deformation better. We assume that those parameter functions are piecewise linear in order not to impose any shape continuity constraints on the LV shape. In other words, the model deforms based on the motion dictated by the SPAMM data and not on the imposition of constraints such as artificial elastic properties (it is impossible with the current non-invasive techniques to measure the viscoelastic properties of the LV for a particular patient in close to real time). Note that it is the same technique used for surface models defined in Park *et al.* (1994, 1995), except that the space of material coordinates  $\mathbf{u}$  is three dimensional, namely  $\mathbf{u} = (u, v, w)$ , instead of two dimensional  $\mathbf{u} = (u, v)$ .

### 4.1 Geometric Definition of the Model

To create a volumetric model for the LV with material coordinates  $\mathbf{u} = (u, v, w)$ , we first define an inertial frame of reference  $\Phi$  and we express the positions on our model by a vector-valued, time-varying function  $\mathbf{x}(\mathbf{u}, t) = (x(\mathbf{u}, t), y(\mathbf{u}, t), z(\mathbf{u}, t))^T$ , where  $^T$  denotes transposition. We also set up a non-inertial, model-centered reference frame  $\phi$  and express the position of

a point on the model as

$$\mathbf{x} = \mathbf{c} + \mathbf{R}\mathbf{s}, \quad (1)$$

where the center of the model  $\mathbf{c}(t)$  is the origin of  $\phi$  and the rotation matrix  $\mathbf{R}(t)$  gives the orientation of  $\phi$  relative to  $\Phi$  with a reference shape  $\mathbf{s}$ . Thus,  $\mathbf{s}(\mathbf{u}, t)$  gives the positions of points on the model relative to the model frame. To model the shape of the LV through  $\mathbf{s}$ , we first define a generalized volumetric primitive  $\mathbf{e}$  as follows<sup>3</sup>:

$$\mathbf{e} = a_0 w \begin{pmatrix} a_1(\mathbf{u}) \cos u \cos v \\ a_2(\mathbf{u}) \cos u \sin v \\ a_3(\mathbf{u}) \sin u \end{pmatrix}, \quad (2)$$

where  $-\frac{\pi}{2} \leq u \leq \frac{\pi}{4}$ ,  $-\pi \leq v < \pi$ ,  $w > 0$ ,  $a_0 > 0$ , and  $0 \leq a_1(\mathbf{u}), a_2(\mathbf{u}), a_3(\mathbf{u}) \leq 1$ .  $a_0$  is a scale parameter and  $a_1$ ,  $a_2$  and  $a_3$  are the aspect ratio parameter functions along the  $x$ -,  $y$ - and  $z$ -axes, respectively. Given the above defined primitive  $\mathbf{e} = (e_1, e_2, e_3)^\top$ , we define the parameterized twisting along the  $z$ -axis, and offset deformations which allow the axis to be non-straight in the  $x$  and  $y$  directions. The resulting global shape  $\mathbf{s}$  is then expressed as follows:

$$\mathbf{s} = \begin{pmatrix} e_1 \cos(\tau(\mathbf{u})) - e_2 \sin(\tau(\mathbf{u})) + e_{1_o}(\mathbf{u}) \\ e_1 \sin(\tau(\mathbf{u})) + e_2 \cos(\tau(\mathbf{u})) + e_{2_o}(\mathbf{u}) \\ e_3 \end{pmatrix}, \quad (3)$$

where  $\tau(\mathbf{u})$  is the twisting parameter function along the  $z$ -axis, and  $e_{1_o}(\mathbf{u})$  and  $e_{2_o}(\mathbf{u})$  are axis-offset parameter functions in the  $x$  and  $y$  directions, respectively. Therefore the deformation parameter vector  $\mathbf{q}_s$  is defined as

$$\mathbf{q}_s = (a_1(\mathbf{u}), a_2(\mathbf{u}), a_3(\mathbf{u}), \tau(\mathbf{u}), e_{1_o}(\mathbf{u}), e_{2_o}(\mathbf{u}))^\top. \quad (4)$$

The parameters,  $\mathbf{q}$ , of the model that we want to recover are

$$\mathbf{q} = (\mathbf{q}_c^\top, \mathbf{q}_\theta^\top, \mathbf{q}_s^\top)^\top, \quad (5)$$

where  $\mathbf{q}_c = \mathbf{c}$ , is the global translation, and  $\mathbf{q}_\theta$ , is the quaternion that corresponds to the global rotation matrix  $\mathbf{R}$ .

## 4.2 Model Dynamics

By incorporating the geometric definition of the models into our physics-based framework, we create dynamic models that deform due to forces exerted from datapoints and conform to the given dataset (Metaxas and Terzopoulos, 1993). In our dynamic formulation, we create a model that has no inertia and comes to rest as soon as all the applied forces equilibrate or vanish. Given that the localization and tracking of SPAMM

<sup>3</sup>it is a generalization of an ellipsoid primitive

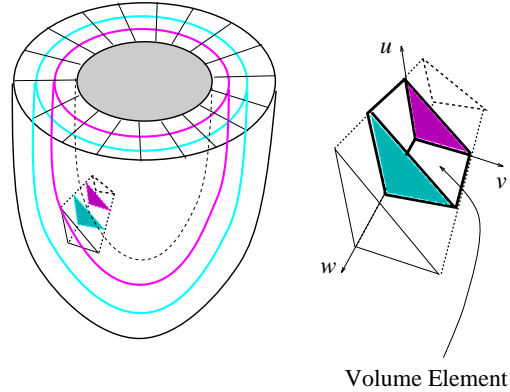


Figure 4: Discretization of the LV model based on Volume elements.

datapoints is relatively accurate, and to avoid undesired smoothness in the solution caused by the incorporation of incorrect elasticity in the model, we assume a zero stiffness matrix<sup>4</sup> so that there is no resistance to deformation. The resulting equation of motion is

$$\mathbf{D}\dot{\mathbf{q}} = \mathbf{f}_q, \quad (6)$$

where  $\mathbf{q}$  is the vector of the model's degrees of freedom,  $\mathbf{D}$  is the damping matrix used as a stabilizing factor, and  $\mathbf{f}_q$  are the generalized forces. These forces are associated with the components of  $\mathbf{q}$  and computed from the 3D force distribution,  $\mathbf{f}$ , applied to the model based on

$$\mathbf{f}_q = \int \mathbf{L}^\top \mathbf{f}, \quad (7)$$

where the Jacobian matrix  $\mathbf{L}$  is defined in Metaxas and Terzopoulos (1993). For fast interactive response, a first-order Euler method (Press *et al.*, 1988) is employed to integrate equation (6).

In computing the correct forces from the data the algorithm exploits the geometry of the motion of the SPAMM datapoints over time. Once these forces are computed, we use a Lagrangian dynamics formulation (Shabana, 1988) to estimate the model parameters.

<sup>4</sup>While we use the above defined deformations, finite elements are often used as an alternative, to model deformations. Possible errors from using finite elements to model the heart wall elasticity arise due to the incorrect computation of the material stiffness matrix when the elasticity of the myocardium which varies spatially is not known. Simplifying assumptions for the elasticity of the myocardium have been attempted. For examples, in the work of Janz and Waldron (1978), the myocardium was approximated with a homogeneous, isotropic and incompressible material, and in the work of Ghista and Hamid (1977), the isoparametric elements are utilized.

## 5 Model Force Computation

The model is discretized based on prismatic volume elements as shown in Fig. 4. The resolution of discretization of the volume of the myocardium depends on how dense the SPAMM datapoints are distributed throughout the volume. In our experiments, we have rather sparse SPAMM datapoints across the myocardium and we therefore tessellated the model so that each volume element has its triangular faces at the inner and outer walls of the LV (see Fig. 5).

We use two types of datapoints to estimate the LV shape and motion, as depicted in Fig. 5. From these data, we compute the corresponding forces on the model depending on their type. Boundary data provide forces for the estimation of the LV shape, while SPAMM datapoints provide forces for the estimation of the volumetric motion of the LV. The following subsections describe the algorithms for extracting and distributing forces from the given dataset.

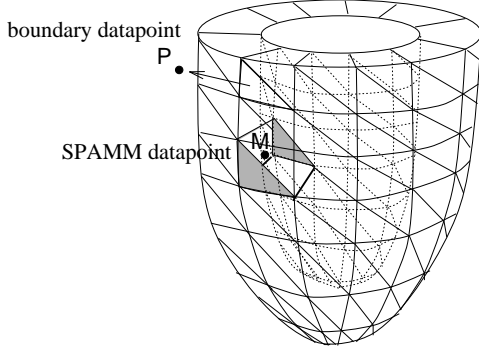


Figure 5: Types of datapoints acting on the model.

### 5.1 Force Computation from Boundary Data

Boundary datapoints simply constrain the shape of the inner and outer walls of the LV and provide no correspondence of points over time. Therefore, the forces from each boundary datapoint  $\mathbf{P}$  to the corresponding model wall (inner or outer) are computed as follows. We approximate each boundary triangular element with a plane. We then determine the element whose distance from  $\mathbf{P}$  is minimum, and the associated intersection point  $\mathbf{Q}$  on the element (see Fig. 6(a)). The force that  $\mathbf{P}$  exerts on the model is

$$\mathbf{f}_P = \gamma_1(\mathbf{P} - \mathbf{Q}), \quad (8)$$

where  $\gamma_1$  is the strength of the force. Then  $\mathbf{f}_P$  is distributed to the nodes  $\mathbf{x}_1, \mathbf{x}_2$  and  $\mathbf{x}_3$  of the associated boundary triangular element based on the formula

$$\mathbf{f}_{\mathbf{x}_i} = m_i \mathbf{f}_P, \quad i = 1, 2, 3, \quad (9)$$

where the  $m_i$  are computed from the solution of the following linear system

$$\sum_i m_i \mathbf{x}_i = \mathbf{Q}, \quad (10)$$

subject to the following constraint

$$\sum_i m_i = 1.0. \quad (11)$$

This constraint is necessary so that the following equation is also true

$$\sum_i \mathbf{f}_{\mathbf{x}_i} = \sum_i m_i \mathbf{f}_P = \mathbf{f}_P. \quad (12)$$

Intuitively, each of the  $m_i$ 's is a weight given to each element node and the vector  $\mathbf{Q}$  is the location of the center of mass of the element's nodes.

### 5.2 Force Computation from SPAMM Data

As opposed to the boundary data, SPAMM data provide correspondence over time of the associated SPAMM datapoints. Due to the way that SPAMM datapoints are defined (see section 3.2), their correspondence over time leads to the computation of forces on the model that are parallel to their corresponding image plane. These forces are computed as follows:

Initially, we assume that the SPAMM datapoints and the model's material points coincide. Let  $\mathbf{M}(t_1)$  be the material point which coincides initially with a SPAMM datapoint  $\mathbf{S}(t_1)$  at time  $t_1$  (see Fig. 7). Let also  $\mathbf{S}(t_2)$  and  $\mathbf{S}(t_3)$  be the corresponding SPAMM datapoints to the point  $\mathbf{S}(t_1)$  at the next two time frames. Then the force on  $\mathbf{M}(t_1)$  from  $\mathbf{S}(t_2)$  is computed as

$$\mathbf{f}_{\mathbf{S}(t_2)} = \gamma_2 [([\mathbf{S}(t_2) - \mathbf{M}(t_1)] \cdot \mathbf{n}_1) \mathbf{n}_1 + ([\mathbf{S}(t_2) - \mathbf{M}(t_1)] \cdot \mathbf{n}_2) \mathbf{n}_2], \quad (13)$$

where  $\gamma_2$  is the strength of the force and  $\mathbf{n}_1, \mathbf{n}_2$ , are the unit normals of the corresponding initial (i.e., at time  $t_1$ ) tagging planes as shown in Fig. 2.

$\mathbf{f}_{\mathbf{S}(t_2)}$  will cause  $\mathbf{M}(t_1)$  to move to a new position  $\mathbf{M}(t_2)$ . Subsequently, the force  $\mathbf{f}_{\mathbf{S}(t_3)}$  on  $\mathbf{M}(t_2)$  from  $\mathbf{S}(t_3)$  will be computed in a similar fashion and it is shown in Fig. 7. The forces  $\mathbf{f}_{\mathbf{S}(t)}$  are always parallel to the corresponding image plane and orthogonal to the initial tagging plane of the SPAMM datapoint. These forces are spring-like forces and are not computed as a result of imposing hard-constraints on the projected motion of a material point. Therefore, when the through-plane motion of a material point is large, the projection of the material point's location on the

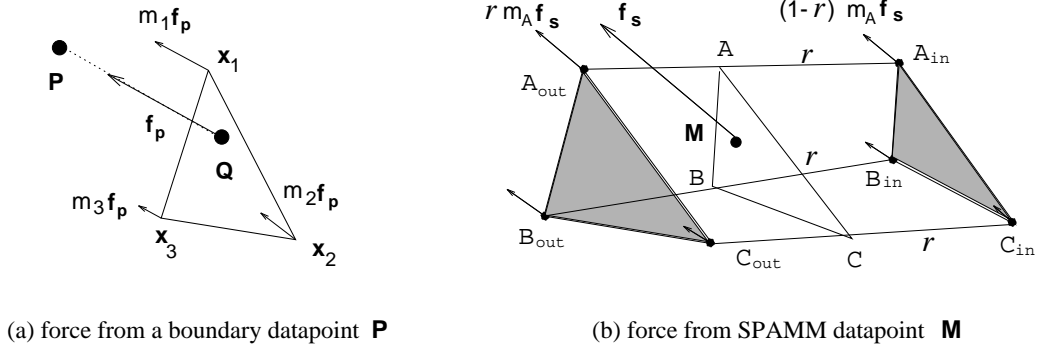
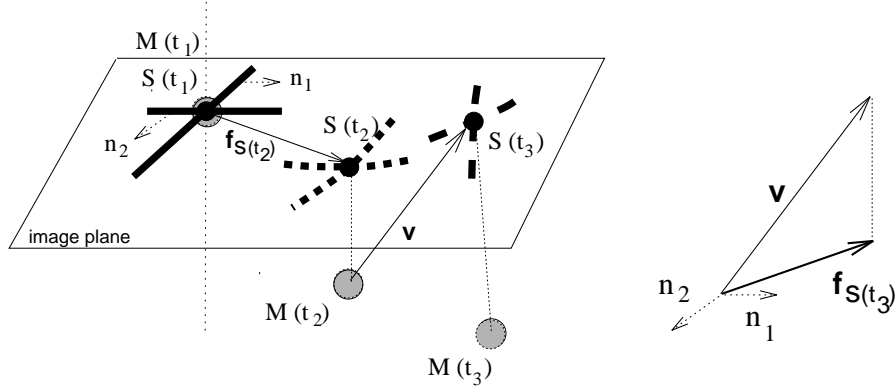


Figure 6: Distributing forces on the model from datapoints.



Forces  $\mathbf{f}_s(t_2)$ ,  $\mathbf{f}_s(t_3)$  from SPAMM points  $\mathbf{S}(t_2)$  and  $\mathbf{S}(t_3)$ , respectively.

Figure 7: Force calculation from SPAMM datapoints.

image plane may not exactly coincide with the location of the corresponding SPAMM datapoint. This is desirable, since in such a case this type of location correspondence is not necessarily valid.

Once we compute these forces, we distribute them to the nodes of the deformable model. These nodal forces will cause the model to deform. We distribute at any time frame  $t_i$ , the computed force  $\mathbf{f}_S$  to the nodes of the prism  $A_{out}B_{out}C_{out}A_{in}B_{in}C_{in}$  within which  $\mathbf{M}$  lies, as follows.

Based on the finite element theory, we compute the nodal positions,  $\mathbf{A}$ ,  $\mathbf{B}$ ,  $\mathbf{C}$ , of the triangle  $ABC$  in which  $\mathbf{M}$  lies such that

$$r = \frac{\mathbf{A} - \mathbf{A}_{in}}{\mathbf{A}_{out} - \mathbf{A}_{in}} = \frac{\mathbf{B} - \mathbf{B}_{in}}{\mathbf{B}_{out} - \mathbf{B}_{in}} = \frac{\mathbf{C} - \mathbf{C}_{in}}{\mathbf{C}_{out} - \mathbf{C}_{in}}, \quad (14)$$

where  $r$  is a scalar. To compute  $r$ , we solve the following cubic scalar equation using the Newton-Raphson method

$$(\mathbf{M} - \mathbf{A}) \cdot ((\mathbf{C} - \mathbf{A}) \times (\mathbf{B} - \mathbf{A})) = 0, \quad (15)$$

where  $\mathbf{A}$ ,  $\mathbf{B}$ ,  $\mathbf{C}$  are computed with respect to  $r$  from equation (14).

The force  $\mathbf{f}_S$  is then extrapolated to the nodes of triangle  $ABC$  based on the same algorithm we used for the force computation from boundary data. The scalars  $m_A$ ,  $m_B$ ,  $m_C$ , correspond to the triangle's nodes  $A$ ,  $B$ ,  $C$ , respectively. Then the forces on the nodes of the prism which lie on the inner and outer walls of the LV are computed as follows (see Fig. 6(b)):

$$\begin{aligned} \mathbf{f}_{N_{out}} &= r m_N \mathbf{f}_S \\ \mathbf{f}_{N_{in}} &= (1-r) m_N \mathbf{f}_S, \end{aligned} \quad (16)$$

where  $N = \{A, B, C\}$ .

The computation of  $r$  which determines the model's material point which corresponds to a SPAMM datapoint is only done once at the beginning of the LV motion estimation. It is the correspondence of SPAMM datapoints over time that allows us to estimate the twisting motion of the LV. In addition, by combining forces from two orthogonal sets of SPAMM datapoints we estimate the full 3D shape and motion of the LV.

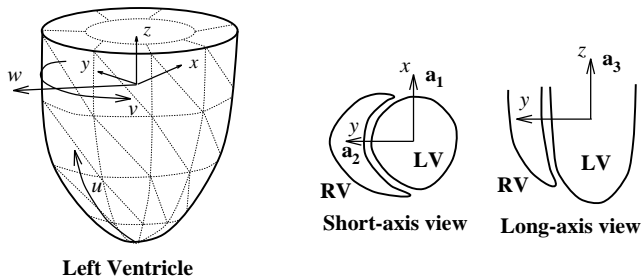


Figure 8: Definition of model's coordinate system.

## 6 Model Parameters

The parameters of the LV model that are estimated during the fitting process reflect the shape changes during systole. The deformable model has six parameter functions  $\mathbf{q}_s$ , to model deformations, as defined in (4), which can be interpreted intuitively without complex post-processing. In addition, the model has global translation  $\mathbf{q}_c$  and global rotation  $\mathbf{q}_\theta$  parameters (see (5)). The initial orientation of the model is important in order to understand the role of each parameter. As depicted in Fig. 8, the short and long axis views initially coincide with the  $xy$ - and  $yz$ - planes in the model frame of reference. The center of the model is chosen at the centroid of the LV with the  $y$ -axis pointing towards the right ventricle (RV). The material coordinates are  $\mathbf{u} = (u, v, w)$ , where  $u$  runs from the apex to the base of the LV,  $v$  starts and ends at the point where the septum is located, and  $w$  is used for the definition of model points between the inner and outer walls of the deformable model. The parameter functions we use are functions of  $\mathbf{u}$ , so that we can model accurately the local variation throughout the LV. As we demonstrate in the following sections, the variation of those parameters with respect to  $u$ ,  $v$ , and  $w$  is chosen so that they are independent.

We now present in detail the interpretation and use of each of the model's parameters. Table 1 summarizes what each parameter function captures during the 3D shape and wall motion estimation of the LV.

Parameters	Representation
$a_1, a_2$	Radial contractions
$a_3$	Longitudinal contraction
$\tau$	Twisting about the long axis
$\epsilon_{1_o}, \epsilon_{2_o}$	Long axis deformation

Table 1: Model Parameters.

### 6.1 Radial Contraction

Since the short axis views coincide initially with the  $xy$ -plane<sup>5</sup>, the parameter functions  $a_1$  and  $a_2$  (which are the aspect ratios along the  $x$ - and  $y$ -axes of the LV model, respectively) will capture the radial contraction motion. Since the  $y$ -axis points towards the septum of the heart, the  $a_2$  parameter captures the motion of the constrained wall, while the  $a_1$  parameter captures the motion of the free wall as shown in Figs. 9(a-b). For each time frame  $t$ , we estimate the values of  $a_1(u, w)$  and  $a_2(u, w)$ , and compute the percentage of the change with respect to their values at end-diastole (ED) which corresponds to the initial time frame (or  $t_{ED}$ ). For example, the graphs shown in Fig. 16(a) are the plot of  $a_1$  computed as follows:

$$\frac{a_1(t) - a_1(t_{ED})}{a_1(t_{ED})} \times 100.$$

Although we do not show in this paper, we can combine parameters  $a_1(u, w)$  and  $a_2(u, w)$ , as one parameter  $\alpha(u, v, w)$  to model the radial contraction of the LV (see Fig. 9(c)). In this case, the geometric definition of the model given in (2) and (3) will become

$$\mathbf{s} = \begin{pmatrix} e_1 \cos(\tau(\mathbf{u})) - e_2 \sin(\tau(\mathbf{u})) \\ e_1 \sin(\tau(\mathbf{u})) + e_2 \cos(\tau(\mathbf{u})) \\ e_3 \end{pmatrix}, \quad (17)$$

where

$$\begin{aligned} e_1 &= a_0 w \alpha(\mathbf{u}) \cos u \cos v, \\ e_2 &= a_0 w \alpha(\mathbf{u}) \cos u \sin v, \\ \text{and } e_3 &= a_0 w a_3(\mathbf{u}) \sin u. \end{aligned} \quad (18)$$

Note that in this case the axis deformation parameters ( $\epsilon_{1_o}$  and  $\epsilon_{2_o}$ ) are not needed, and parameter independence is maintained.

### 6.2 Longitudinal Contraction and Global Translation

Since the long axis views coincide with the  $yz$ -plane, the parameter function  $a_3$  (which is the aspect ratio along  $z$ -axis) will capture the longitudinal contraction motion. However, since we do not have enough time frames over the heart cycle, the estimation of the global translation in the  $z$  direction of the model frame can be arbitrary (the two parameters can't be independently estimated) and may result in the false estimation of especially the longitudinal deformation parameters (the global translation in the  $x$  and the  $y$  directions of the model frame is negligible). Consider the following case

<sup>5</sup>The  $xy$ -plane does deviate over time from the short axis view due to the global rotation of the LV, but not significantly.

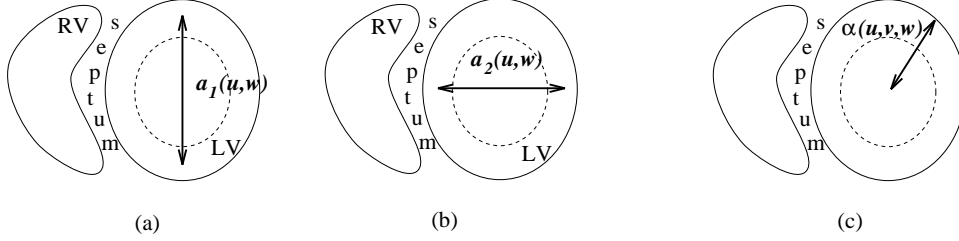


Figure 9: Parameters for radial contraction:  $a_1(u, w)$ ,  $a_2(u, w)$ .

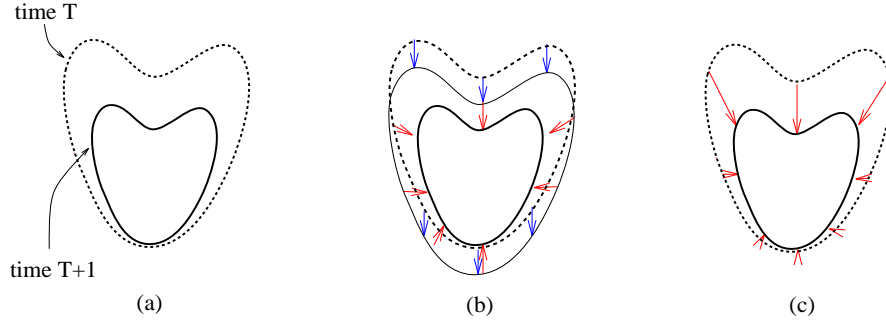


Figure 10: Parameters for longitudinal contraction and global translation.

shown in Fig. 10(a). It is a typical motion of the LV observed at two subsequent time instances ( $T$  and  $T+1$ ), which shows that the motion at the apex of the LV is relatively small. Suppose that the length of the LV is  $10cm$  and  $8cm$ , at times  $T$  and  $T+1$ , respectively. If the origin of the model frame at time  $T$  is at the half way along the LV, the origin would globally translate  $1cm$  at time  $T+1$ . Yet this amount of translation is arbitrary because it depends on where the origin is. Moreover, in this case we would capture a relatively uniform longitudinal contraction from apex to base as shown in Fig. 10(b). This has the result that, even though the combination of translation and longitudinal contraction would give the correct 3D motion of the LV, the longitudinal contraction would lose its intuitive meaning. However, as mentioned above this is an artifact of the sparse sampling over time.

Due to the above sparse sampling, and the fact that we could not observe a significant overall translation of the model in all our datasets, we kept the global translation constant during the fitting process for the subsequent time frames. We therefore capture the LV longitudinal motion as a deformation based on  $a_3$  (see Fig. 10(c)). In our experiments, we compute the actual displacement based on the  $a_3$  parameter as follows:

$$a_{3_d} = a_3(t) \sin(u) - a_3(t_{ED}) \sin(u).$$

We plot the percentage of the changes with respect to the initial length of the LV in order to compare the amount among different LVs. For example, the graphs

shown in Fig. 16(c) are the plot of  $a_3$  computed as follows:

$$\frac{a_{3_d}}{\text{length of the LV}} \times 100.$$

In case there is a pathological case that the LV translates (globally) significantly along the  $z$  axis in addition to contracting, then we can very easily estimate this global translation by simply subtracting from  $a_{3_d}$  the common least amount of deformation from apex to base. However, it is not clear that knowledge of the global translation is clinically useful.

### 6.3 Twisting and Global Rotation

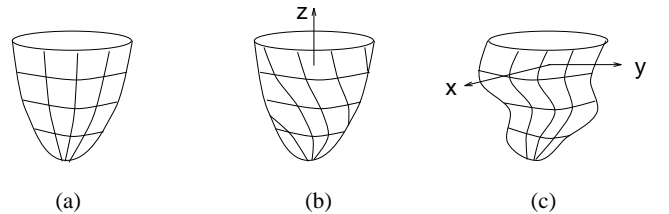


Figure 11: Twisting and long axis deformations.

The twisting parameter function  $\tau(u, v, w)$  captures the twisting about the long axis of the LV as shown in Fig. 11(b). For each location  $w$ , and for each location  $u$ , we allow the parameter to vary along  $v$  in order to obtain the variation of twisting as a function of circumferential position as well. The average of the twisting

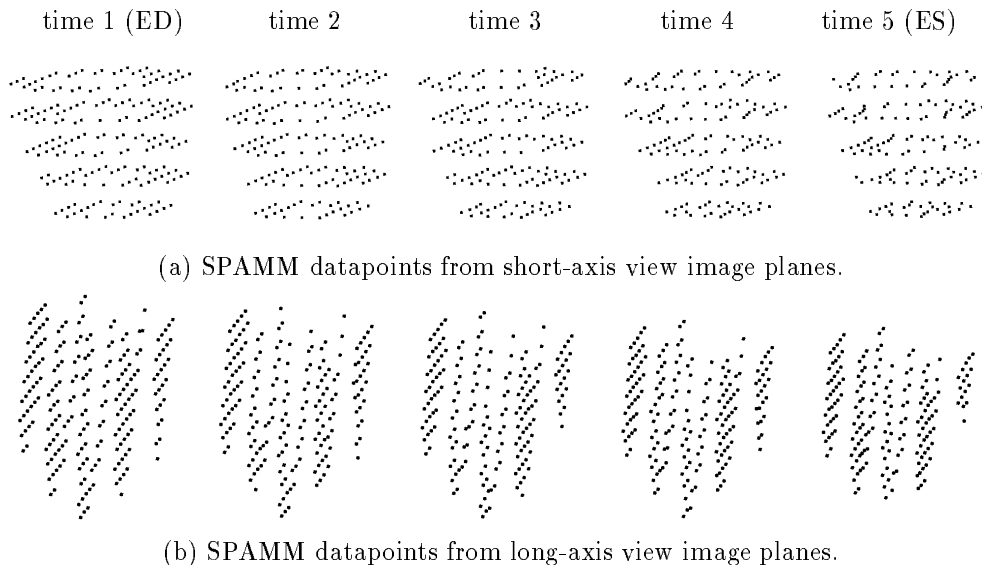


Figure 12: SPAMM datapoint sets.

values at all the circumferential positions for each location  $u$  is plotted in Fig. 16 and Fig. 17. In this way we quantify the twisting motion from the apex to the base of each LV.

At each subsequent time frame, we first estimate the global rotation of the model before estimating the deformation parameters. In this way, we can subtract the global rotation from the twisting deformation, and therefore estimate the overall tilting of the LV.

The global rotation of our model is expressed as a quaternion. This results in numerically more robust estimation of global rotation during model fitting to the data (Metaxas, 1992). In addition, from the quaternion we can compute very efficiently the corresponding rotation matrix  $\mathbf{R}$  that we use to compute the nodal positions  $\mathbf{x}$  based on (1).

## 6.4 Long Axis Deformation

By having the axis-offset parameters  $e_{1_o}(u, w)$  and  $e_{2_o}(u, w)$ , we allow the centroid of each cross section at a different location along the long-axis of the LV to displace globally in the  $xy$ -plane (see Fig. 11(c)). In this way we can capture the shape of the LV accurately, and at the same time observe the bending of the LV, if any, without using any special function for the bending.

## 6.5 Ejection-fraction and Other Parameters

It is also very important to mention that our technique for constructing these deformable models is general and we can therefore add other global deformations such as

bending and shearing. However, for the experiments we present the above described parameters were adequate.

If needed, it is also possible to do strain analysis as follows. Based on the extracted model parameters, we first compute the positions,  $\mathbf{x}_i$ , of the element nodes from (1) and then we apply the standard strain computation procedure as in Young *et al.* (1994).

Finally, by adapting Gauss' theorem (O'Neil, 1987) we can accurately calculate over time the volume of the blood pool, and therefore compute ejection-fraction.

## 7 Implementation of Model Fitting Procedure

We have applied our approach to MRI-SPAMM data of LVs obtained at the Department of Radiology of the University of Pennsylvania. As discussed in Section 3.2, in order to estimate the 3D left ventricular wall motion, we used two sets of SPAMM datapoints obtained from mutually orthogonal image planes (short-axis and long-axis views). We used data from ten image planes, five from short-axis view planes, and another five from long-axis view planes. These image planes span the spatial extent of the LV. Furthermore, for each image plane, we have datasets over five time sequences during systole (from end-diastole to end-systole). Therefore, in total,  $10 \times 5 = 50$  datasets of 2D images, containing time-varying datapoints of the LV, were utilized. Fig. 12 shows a set of SPAMM datapoints extracted from the MR images of a normal LV. Since some of the SPAMM datapoints on the image plane disappear and/or reappear at subsequent times, we used at every

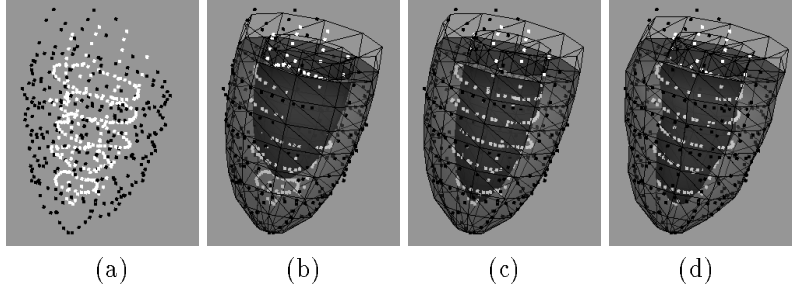


Figure 13: Initial model shape recovery from boundary data.

time frame only those points which have a corresponding point at the previous time frame. Therefore, the number of *active* points decreases towards end-systole.

From each image, we also extracted the boundary datapoints representing inner and outer walls. Through the following experiment we give the details of the model fitting procedure to the boundary and the SPAMM datapoints.

Starting from a generalized ellipsoid, we first estimate the shape of the LV at end-diastole from the boundary dataset. Then we fit the LV model to the data from subsequent time frames gradually up to end-systole and we estimate its motion over time. Note that the fitting process for each time frame takes approximately 45 seconds on a Silicon Graphics R4400 Indigo workstation.

## 7.1 Model Fitting to Boundary Datapoints at End-Diastole

Based on the boundary datapoints from the inner and outer walls, we first recover the shape of the LV at time 1 (i.e., end-diastole). This is done by first overlaying a simple volumetric model, which resembles a volumetric ellipsoid, onto the data (Fig. 13(a) shows all boundary datapoints at time 1, where black dots and white dots are on the outer and inner walls, respectively.). Initially, the model frame is placed at the center of mass of the boundary datapoints. The forces acting on the model will cause it to translate and to rotate to find a suitable position and orientation.

Then, based on the computation of boundary forces, the nodes on the inner and outer walls of the model are pulled towards the inner and outer boundary datapoints, respectively. As a result of these forces, the model parameter functions change so that the model conforms to the dataset. When all applied forces equilibrate or vanish, or the error of fit (the distance between a datapoint and the model surface) falls within an acceptable tolerance specified by the user, the model comes to rest. For efficient and effective model fitting, we come up with the following fitting schedule:

1. The initial model has constant parameter functions; in particular,  $a_1(\mathbf{u}) = c_1$ ,  $a_2(\mathbf{u}) = c_2$ ,  $a_3(\mathbf{u}) = c_3$  and  $\tau(\mathbf{u}) = e_{1_o}(\mathbf{u}) = e_{2_o}(\mathbf{u}) = 0$ , where  $0 < c_1, c_2, c_3 < 1$ , for all  $\mathbf{u} = (u, v, w)$ . The model rotates and translates to find its optimal location for the model center in the reference frame, while estimating  $c_1$ ,  $c_2$  and  $c_3$ . We also estimate the value of the material coordinate  $w$  for the inner and outer walls at this stage (Fig. 13(b) :  $w_{in} = 0.896$  and  $w_{out} = 1.368$ ).
2. Once the fitting of the model in the first step is completed and we have estimated  $w$  for the inner and outer walls, the  $a_1$ ,  $a_2$  and  $a_3$  parameters are allowed to vary with respect to  $w$  only, so that we can recover the wall thickness more accurately (Fig. 13(c) :  $a_1(w_{out}) = 0.360$ ,  $a_1(w_{in}) = 0.282$ ,  $a_2(w_{out}) = 0.341$ ,  $a_2(w_{in}) = 0.276$ ,  $a_3(w_{out}) = 0.807$ , and  $a_3(w_{in}) = 0.924$ ).
3. Finally, the parameters are allowed to vary also in  $u$  to estimate the non-symmetrical shape of the LV. We first estimate the parameter functions  $a_1(u, w)$ ,  $a_2(u, w)$  and  $a_3(u, w)$  and then  $e_{1_o}(u, w)$  and  $e_{2_o}(u, w)$  (Fig. 13(d)). Note that the twist parameter  $\tau$  is activated when the datapoints from next time frame (time 2) are loaded.

## 7.2 Registration of SPAMM Datapoints to the Model

After the model fits the initial boundary data at end-diastole (ED), we use it to fit data from subsequent time frames till end-systole (ES). We first read in the SPAMM datapoints at ED in order to register the locations of SPAMM datapoints which coincide with material points. For each SPAMM datapoint, we find the volume element which encloses the datapoint, and compute  $r$  and  $m_N$  as described in Section 5.2. The values of  $r$  and  $m_N$  give the relative location of each material point marked on the model with respect to the enclosed volume element. Therefore we can always locate the

material point regardless of how the volume element is deformed.

### 7.3 Model Fitting to Datapoints Over Time

The SPAMM datapoints at time 2 are loaded onto the previously fitted model (time 1). The model deforms due to the SPAMM data forces, as described in Section 5.2. The combination of forces from the SPAMM datapoints in two orthogonal sets allow us to recover the deformation of the model in all three components, effectively recovering the missing through-plane motion (see Fig. 15 and Fig. 18). Once the model comes to rest, the SPAMM datapoints at time 3 are loaded onto the fitted model of time 2. And we repeat the process for up to end-systole. The deformation from ED to ES is captured in the parameter functions. By plotting the parameter functions over time, we can characterize and quantify the motion of the LV.

Note that we also utilize boundary datapoints during the subsequent time fittings. We first estimate rigid motion using both boundary and SPAMM datapoints, and then the deformation using only SPAMM datapoints.

## 8 Experimental Results

In the following experiments we present our LV shape and motion analysis results for normal and abnormal LVs with hypertrophic cardiomyopathy (**htcm**).

Fig. 14 shows model fitting results for a normal LV over 5 time frames from end-diastole (ED) to end-systole (ES). The top row shows a view from the base of the LV of the fitted model. The twisting of the inner wall (shown in white) is obvious. The middle row shows a side view of the model, while the last row is similar to the first row and shows a view of the model from the apex. We can easily observe the longitudinal contraction as well as the radial contraction. The combination of computed forces from the SPAMM datapoints from two orthogonal planes allows us to recover the deformation of the model in 3D.

Fig. 15 shows the fitted model superimposed on the SPAMM datapoints over 5 time frames. SPAMM datapoints are denoted with black dots, while the corresponding model material points are denoted with white dots. Initially, the SPAMM datapoints coincide with the material points on the model (therefore, only black dots are shown in the Fig. 15(a)). The first two rows show the model with superimposed short-axis SPAMM datapoints (Fig. 12(a)), and long-axis SPAMM datapoints (Fig. 12(b)), respectively. The last row shows both sets of SPAMM datapoints. We can observe that

the material points move in 3D space, thus recovering the through-plane motion, while the image planes (where black dots are located in Fig. 15) are stationary.

Fig. 18 shows a top portion of the model at the end-systole. The red dots indicate the SPAMM datapoints<sup>6</sup> at end-diastole, which coincide with the corresponding material points. The yellow dots are the SPAMM datapoints at the end-systole, and their motion paths over time are shown in green. The light blue dots are the corresponding material points at the end-systole. The 3D motion paths of the material points during systole are shown in white. Notice that at every instant the projection of the material point location on the image plane approximately coincides with the location of the SPAMM datapoint.

### 8.1 Parameter Graphs

Fig. 16 shows graphs of the extracted model parameters as functions of  $u$  (i.e., varying along the long axis of the LV) at the inner and outer walls. In general, the contraction and the twisting deformation are more significant on the inner LV wall (Figs. 16(g-j)) compared to the outer wall (Figs. 16(a-d)). The difference in the corresponding parameter values is obvious. The graphs allow us to quantify the motion and shape changes of the LV during systole. For example, by studying the graphs in Figs. 16(a,b), we can conclude that the overall percent changes of the magnitude of radial contraction of the outer wall during systole is approximately 15 – 20%. However, towards the base of the LV the contraction along the  $y$  axis (it is approximately 10% from Fig. 16(b)) is less than the contraction along the  $x$  axis (it is approximately 17% from Fig. 16(a)) making the base look more elliptical. From Fig. 16(d) we can quantify the twisting motion of the outer wall during systole to approximately 14 degrees total from base to apex. The graph shows a small amount of global rotation before the twisting occurs.<sup>7</sup> It is not easy to see this kind of subtle motion when one watches the model contract and twist on the monitor. Figs. 16(e, f, k, l) show the estimation results for the long axis deformation, which represent small changes and are not significant. By having the graphs of the parameter functions plotted in conjunction with the animation, we can quantify and easily characterize the detailed motion of the deforming model over time.

In Fig. 17 we show fitting results to SPAMM data from an abnormal LV with hypertrophic cardiomyopathy (**htcm**). By comparing the corresponding graphs

<sup>6</sup>It is a subset of SPAMM datapoints from a short-axis view image plane.

<sup>7</sup>Compare the changes in the parameter values in Figs. 16(d,j) from time 1 to time 2 with the changes from time 2 to time 3.

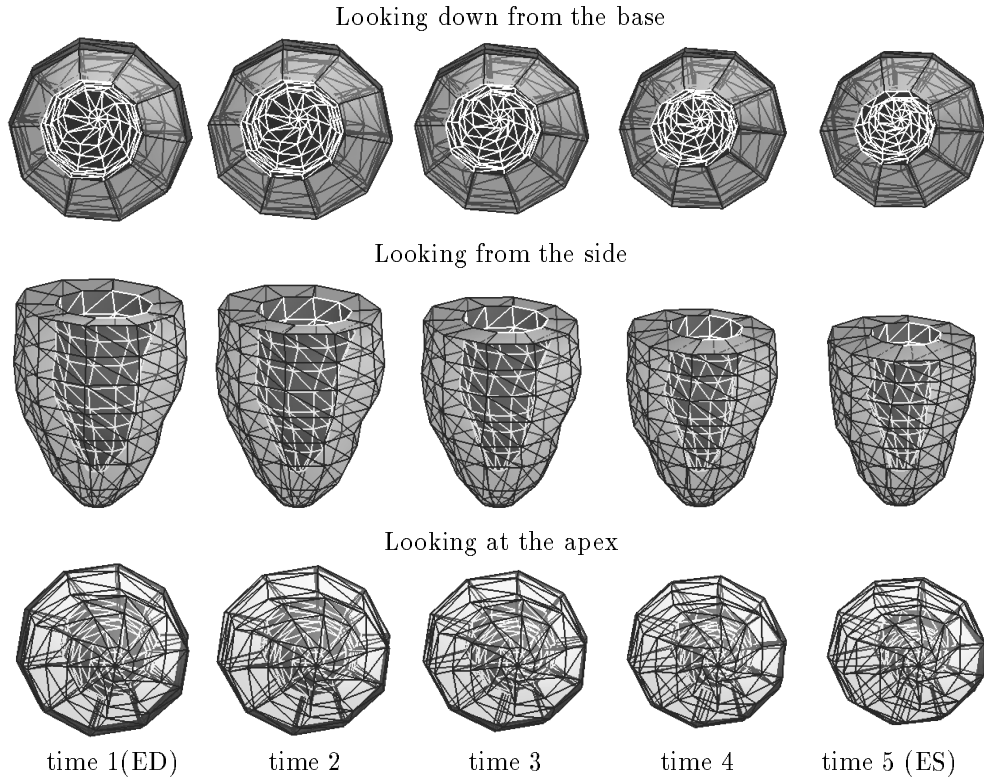


Figure 14: Fitted models during systole.

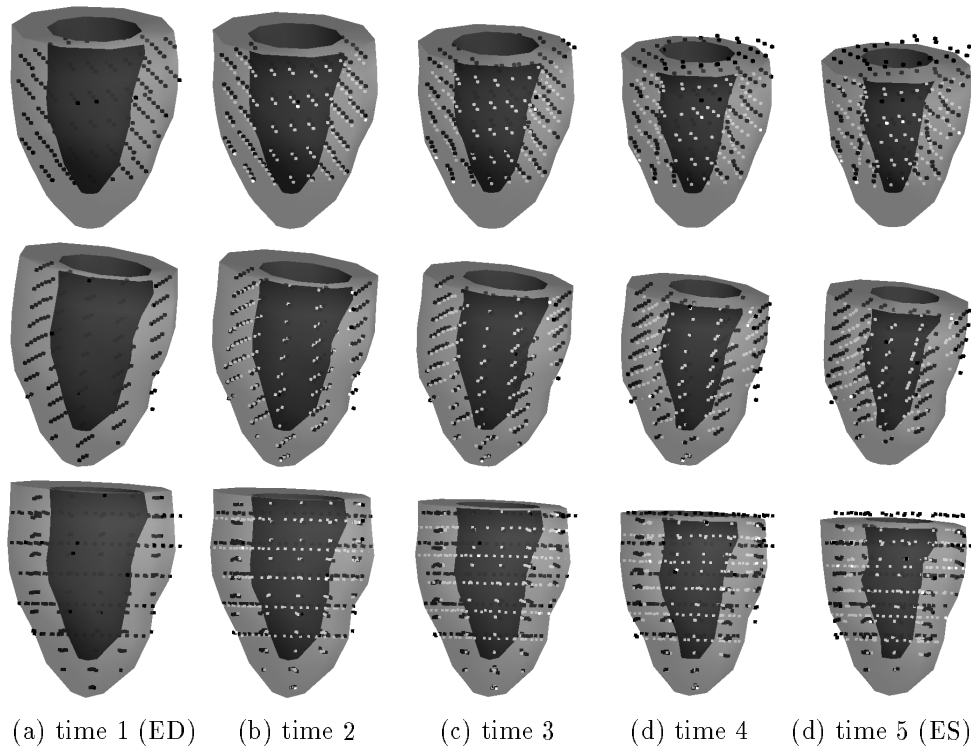


Figure 15: Fitted models during systole with SPAMM datapoints and material points.

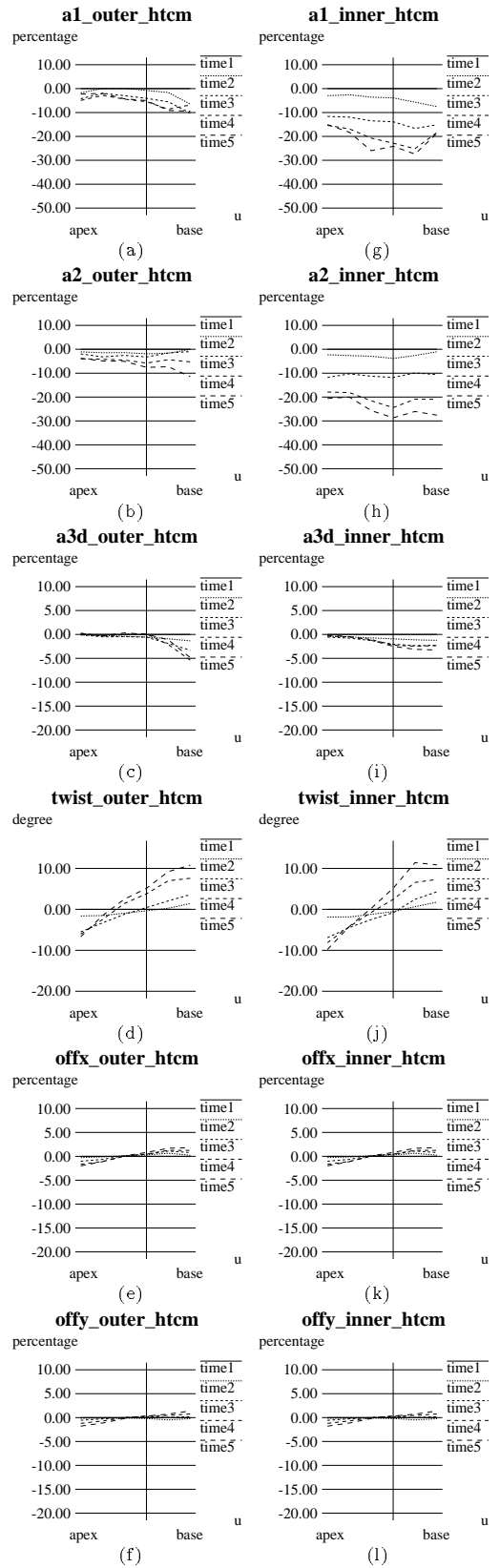
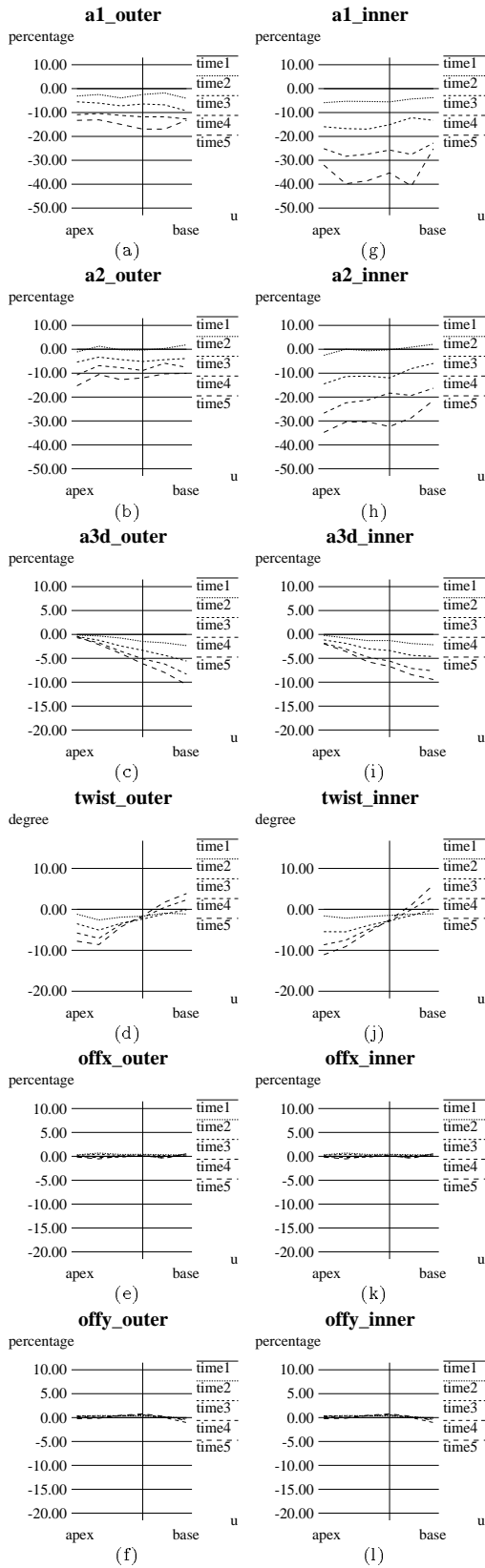


Figure 16: Extracted model parameters as functions of  $u$  (Normal LV).

Figure 17: Extracted model parameters as functions of  $u$  (Abnormal LV).

we can observe that the abnormal heart does not contract as much as the normal heart (especially towards the apex), but twists more, and has a bigger long axis deformation. This latter deformation corresponds to a spatial bending of the LV.

In Fig. 19 we illustrate in color the twisting motion of the two LVs at two short axis views (A and B) and one long axis view (C). In our coloring method, white corresponds to zero twist, yellow to red corresponds to positive (clockwise) twist, and green to blue corresponds to negative (counter-clockwise) twist. During systole, for each LV (normal and abnormal) the first two rows on the left illustrate the variation in twisting on the two short axis views, while the third row on the left shows the variation in twisting on the long axis view (notice that the  $y$  axis always points towards the septum). Finally, for each of the two LVs, the rows on the right depict at end-systole the twisting motion of the LV on the inner and outer walls (top row), and on the A, B and C cross-sections (bottom row) where white meshes depict the cross-section at end-diastole and black lines depict point correspondences. The maximum twists are depicted in red (10 degrees) and blue (-10 degrees). From this coloring we can clearly visualize the nonuniform twisting motion throughout each of the LVs. It also becomes clear that the abnormal LV twists more and its twisting motion is more non-uniform. Both the normal and the abnormal LVs twist more towards the free-wall (negative  $y$  direction). We can also observe the changes in the myocardium thickness during systole. The above coloring is also adapted for each of the rest parameter functions.

Based on Gauss' theorem (O'Neil, 1987), we also calculated the volume of the blood pool over time to compute ejection-fraction. The ejection-fraction of the normal LV was 61%, while for the abnormal it was 52%.

All the above presented results verify quantitatively qualitative knowledge about the LV known to physicians. We plan to conduct a series of experiments with normal and abnormal hearts with various types of disease in order to investigate the relationship between the extracted parameter functions and heart disease.

## 8.2 Video: Estimation of the LV Shape and Motion from MRI-SPAMM

The accompanying movie demonstrates the following phases of the shape and motion estimation of a normal LV.<sup>8</sup>

<sup>8</sup>The movie plays at 6 frames/second.

1. **[25-108 (14 sec)]**<sup>9</sup> We show one short and one long axis views of a beating heart captured by MRI-SPAMM. The SPAMM datapoints are the intersections of the black lines within the walls of the LV. As mentioned above, based on active contours we can track over time the motion of the SPAMM datapoints on each of the views.
2. **[109-162 (9 sec)]** This section demonstrates the process of fitting a volumetric deformable model to the initial boundary data at end-diastole (ED). The resulting model becomes the initial model for the LV motion estimation during systole.
3. **[163-246 (14 sec)]** This section demonstrates the process of registering the SPAMM datapoints to the recovered LV model at ED. In other words, the corresponding material points which coincide with SPAMM datapoints at ED are marked on the model. Since there are no SPAMM datapoints in the top-most part of the model (i.e. the base of LV) in this particular case, the model is adjusted to exclude its top-most part for accurate estimation of the motion and the ejection fraction of the LV. Then we show several views of the recovered shape.
4. **[247-336 (15 sec)]** This section demonstrates one instance of the motion estimation during systole. The initial model shown in this segment is the recovered model at time 2, and it deforms due to the forces from SPAMM datapoints at time 3. The 2D force components acting on the model are depicted. The final model in this segment is the model at time 3.
5. **[337-408 (12 sec)]** This section demonstrates the LV shape and motion estimation results from time 1 (ED) to time 5 (ES). For demonstration purposes, we show in sequence the outer surface mesh, the inner surface mesh, and then the volumetric model.
6. **[409-534 (21 sec)]** We plot extracted parameter graphs for radial contraction ( $a_1$ ), longitudinal contraction ( $a_3$ ) and twist ( $\tau$ ), from ED to ES (in 5 time frames). Each parameter is plotted as a function of  $u$ , where we can quantify their variations from the apex to the base of the LV. We plot parameter values at the outer and the inner LV walls with different colors for a comparison.
7. **[535-612 (13 sec)]** This section demonstrates the recovery of the through plane motion of material

<sup>9</sup>The first set of numbers denote the frame numbers in the video sequence, and the number in parentheses denotes the frame playback duration in seconds.

points at a certain short axis view. It shows the 3D paths of the material points and the planar motion paths (on the short axis plane) of the corresponding SPAMM datapoints.

## 9 Conclusion

We have developed a new class of physics-based volumetric deformable models whose global parameters are functions to estimate and analyze the LV shape and motion in a *clinically useful manner*. In addition we have shown how to automatically incorporate force constraints from MRI-SPAMM data into our deformable model, and have developed a set of visualization tools to improve the presentation of our analysis results. We have demonstrated that we are able to estimate the complex volumetric shape and motion of the LV and compare the epicardial and endocardial wall motions. Based on these initial very encouraging results we plan to do a series of future studies to identify what is normal and what is abnormal heart motion, and more importantly to be able to link in a quantitative way the LV motion with a particular illness. Finally, we also plan to conduct studies with deformable phantoms to further evaluate the accuracy of our technique.

## Acknowledgments

We are very grateful to Dr. Alistair Young at the University of Auckland, New Zealand for his helpful comments, support and encouragement. We would also like to thank Dr. Kenneth Fellows at the Children's Hospital of Philadelphia for partially supporting the first author. This work was supported by grants from NSF and NIH.

## References

- Arts T., Veenstra P.C., Reneman R.S., (1982) "Epicardial deformation and left ventricle wall mechanics during ejection in the dog," *Am. J. Physiol.*, **243**, H379-H390.
- Arts T., Hunter W.C., Douglas A., Muijtjens M.M., Reneman R.S., (1992) "Description of the deformation of the left ventricle by a kinematic model," *J Biomechanics*, **25**(10), 1119-1127.
- Arts T., Hunter W.C., Douglas A.S., Muijtjens A.M.M., Corsel J.W., Reneman R.S., (1993) "Macroscopic Three-Dimensional Motion Patterns of The Left Ventricle," *Advances in Experimental Medicine and Biology*, **346**, 383-392.
- Axel L., Dougherty L., (1989) "Heart wall motion: Improved method of spatial modulation of magnetization for MR imaging," *Radiology*, **172**, 349-350.
- Axel L., Gonçqalves F., Bloomgarden D., (1992) "Regional heart wall motion: Two-dimensional analysis and functional imaging of regional heart wall motion with magnetic resonance imaging," *Radiology*, **183**, 745-750.
- Axel L., Bloomgarden D., Cheng C-N, Kraitchman D., Young A.A., (1993) "SPAMMVU: A Program for the Analysis of Dynamic Tagged MRI," in: Book of Abstracts: Society of Magnetic Resonance in Medicine, 724.
- Amini A., Duncan J., (1991) "Pointwise tracking of Left-Ventricular Motion in 3D," Proc. IEEE Workshop on Visual Motion, Princeton, NJ, 294-298.
- Azhari H., Buchalter M., Sideman S., Shapiro E., Beyar R., (1992) "A Conical Model to Describe the Nonuniformity of the Left Ventricular Twisting Motion," *Annals of Biomedical Engineering*, **20**, 149-165.
- Bardinet E., Ayache N., Cohen L.D., (1994) "Fitting of Iso-Surfaces Using Superquadrics and Free-Form Deformations," Proceedings of IEEE Workshop on Biomedical Image Analysis, Seattle, WA, 184-193.
- Beyar R., Sideman S., (1985) "Effect of the twisting motion on the non-uniformities of transmural fiber mechanics and energy demands - A theoretical study," *IEEE Trans. Biomed. Eng.*, **32**, 764-769.
- Brower R.W., Katen H.T., Meester G.J., (1978) "Direct method for determining regional myocardial shortening after bypass surgery from radiopaque markers in man," *Am. J. Cardiol.*, **41**, 1222-1229.
- Chen C.W., Huang T.S., (1990) "Epicardial Motion and Deformation Estimation from Coronary Artery Bifurcation Points," Proceedings of 3rd International Conference on Computer Vision, Osaka, Japan, 456-459.
- Cohen L.D., Cohen I., (1990) "A Finite Element Method Applied to New Active Contour Models and 3D Reconstruction from Cross Sections," Proc. 3rd International Conference on Computer Vision, Osaka, Japan, 587-591.
- Denney T.S. Jr., Prince J.L., (1994) "3D Displacement Filled Reconstruction on an Irregular Domain from Planar Tagged Cardiac MR Images," Proc. Workshop on Motion of Non-Rigid and Articulated Objects, Austin, TX, 172-177.
- Fischer S.E., McKinnon G.C., Scheidegger M.B., Prins W., Meier D., Boesiger P., (1994) "True Myocardial Motion Tracking," *Magnetic Resonance in Medicine*, **31**, 401-413.
- Friboulet D., Magnin I.E., Revel D., (1992) "Assessment of a model for overall left ventricular three-dimensional motion from MRI data," *Intl. Journal of Cardiac Imaging*, **8**, 175-190.
- Friboulet D., Magnin I.E., Mathieu C., Pommert A., Hoehne K.H., (1993) "Assessment and visualization of the curvature of the left ventricle from 3D medical images," *Computerized Medical Imaging and Graphics*, **17**(4/5), 257-262.

- Ghista D.N., Hamid M.S., (1977) "Finite Element Stress Analysis of the Human Left Ventricle whose irregular shape is developed from single plane cineangiogram," *Computer Programs in Biomedicine*, **7**, 219-231.
- Guccione J.M., McCulloch A.D., (1991) "Finite Element Modeling of Ventricular Mechanics," in: L. Glass, P. Hunter, A. McCulloch, eds. *Theory of Heart: biomechanics, biophysics, and nonlinear dynamics of cardiac function*, New York, Springer-Verlag, 121-144.
- Harrison D.C., Goldblatt A., Braunwald E., Glick G., Mason D.T., (1963) "Studies on cardiac dimensions in intact unanesthetized man. 1. Description of techniques and their validation," *Circ. Res.*, **13**, 448-455.
- Huang W.C., Goldgof D., (1993) "Adaptive-Size Meshes for Rigid and Nonrigid Shape Analysis and Synthesis," *IEEE Transactions on Pattern Analysis*, **15**(6), 611-616.
- Janz R.F., Waldron R.J., (1978) "Predicted Effect of Chronic Apical Aneurysms on the Passive Stiffness of the Human Left Ventricle," *Circ. Res.*, **42**(2), 255-263.
- Kambhamettu C., Goldgof D., (1992) "Point Correspondence Recovery in Non-rigid Motion," Proceedings of IEEE Conference on Computer Vision and Pattern Recognition, Champaign, Illinois, 222-227.
- Kass M., Witkin A., Terzopoulos D., (1988) "Snakes: Active Contour Models," *International Journal of Computer Vision*, **1**(4), 321-331.
- Kim H.C., Min B.G., Lee M.M., Seo J.D., Lee Y.W., Han M.C., (1985) "Estimation of local cardiac wall deformation and regional wall stress from biplane coronary cineangiograms," *IEEE Trans. Biomed. Eng.*, **32**, 503-511.
- McInerney T., Terzopoulos D., (1993) "A Finite Element Model for 3D Shape Reconstruction and Nonrigid Motion Tracking," Proc. 4th International Conference on Computer Vision, Berlin, Germany, 518-523.
- Meier G.D., Bove A.A., Santamore W.P., Lynch P.R., (1980) "Contractile function in canine right ventricle," *Am. J. Physiol.*, **239**, H794-H804.
- Metaxas D., (1992) Physics-Based Modeling of Nonrigid Objects for Vision and Graphics, Ph.D. Thesis, Department of Computer Science, University of Toronto.
- Metaxas D., Terzopoulos D., (1993) "Shape and Nonrigid Motion Estimation Through Physics-Based Synthesis," *IEEE Trans. Pattern Analysis and Machine Intelligence*, **15**(6), 569-579.
- Mishra S.K., Goldgof D.B., (1991) "Motion Analysis and Modeling of Epicardial Surfaces from Point and Line Correspondences," Proc. of IEEE Workshop on Visual Motion, Princeton, NJ, 300-305.
- Moore C., O'Dell W., McVeigh E., Zerhouni E., (1992) "Calculation of three-dimensional left ventricular strains from biplanar tagged MR images," *J Mag Res Imag*, **2**, 165-175.
- Nastar C., Ayache N., "Spatio-temporal analysis of non-rigid motion from 4D data," Proc. Workshop on Motion of Non-Rigid and Articulated Objects, Austin, TX, November 1994: 146-151.
- O'Dell W.G., Moore C.C., McVeigh E.R., (1993) "Displacement field fitting approach to calculate 3d deformations from parallel-tagged MR images," *J. Magn. Reson. Imag.*, **3**(P), P208.
- O'Neil P.V., *Advanced engineering mathematics*, 2nd ed., Belmont, Calif., Wadsworth Pub. Co., 1987.
- Park J., Metaxas D., Young A., (1994) "Deformable Models with Parameter Functions: Application to Heart-Wall Modeling," Proc. IEEE Computer Vision and Pattern Recog., Seattle, WA, 437-442.
- Park J., Metaxas D., Young A., Axel L., (1994) "Model-based Analysis of Cardiac Motion from Tagged MRI Data," Proc. Seventh Annual IEEE Symposium on Computer-Based Medical Systems, Winston-Salem, North Carolina, 40-45.
- Park J., Metaxas D., Axel L., (1995) "Volumetric Deformable Models with Parameter Functions: A New Approach to the 3D Motion Analysis of the LV from MRI-SPAMM," Proceedings of 5th International Conference on Computer Vision, Cambridge, Massachusetts, 700-705.
- Park J., Metaxas D., Young A.A., Axel L., (1996) "Deformable Models with Parameter Functions for Cardiac Motion Analysis from Tagged MRI Data," *IEEE Trans. on Medical Imaging*, in press.
- Pentland A., Horowitz B., (1991) "Recovery of Nonrigid Motion and Structure," *IEEE Pattern Analysis and Machine Intelligence*, **13**(7), 730-742.
- Pentland A., Horowitz B., Sclaroff S., (1991) "Non-Rigid Motion and Structure from Contour," Proc. of IEEE Workshop on Visual Motion, Princeton, NJ, 288-293.
- Press W.H., Flannery B.P., Teukolsky S.A., Vetterling W.T., (1988) *Numerical Recipes in C: The Art of Scientific Computing*, Cambridge, UK, Cambridge University Press.
- Rankin J.S., McHale P.A., Artentzen C.E., Ling D., Greenfield J.C., Anderson R.W., (1976) "The three-dimensional dynamic geometry of the left ventricle in the conscious dog," *Circ. Res.*, **39**, 304-313.
- Rogers W., Shapiro E., Weiss J., Buchalter M., Rademakers F., Weisfeldt M., Zerhouni E., (1991) "Quantification of and correction for left ventricular systolic long-axis shortening by magnetic resonance tissue tagging and slice isolation," *Circulation*, **84**, 721-731.
- Sclaroff S., Pentland A., (1994) "On Modal Modeling for Medical Images: Underconstrained Shape Description and Data Compression," Proceedings of IEEE Workshop on Biomedical Image Analysis, Seattle, WA, 70-79.
- Shabana A.A., (1988) *Dynamics of Multibody Systems*, New York, A Wiley-Interscience Publication.

- Shi P., Amini A., Robinson G., Sinusas A., Constable C.T., Duncan J., (1994) "Shape-based 4D Left Ventricular Myocardial Function Analysis," Proc. of IEEE Workshop on Biomedical Image Analysis, Seattle, WA, 88-97.
- Shi P., Robinson G., Constable T., Sinusas A., Duncan J., (1995) "A Model-Based Integrated Approach to Track Myocardial Deformation Using Displacement and Velocity Constraints," Proceedings of 5th International Conference on Computer Vision, Cambridge, Massachusetts, 687-692.
- Tennant R., Wiggers C.J., (1935) "The effect of coronary occlusion on myocardial contraction," *Am J Physiol*, **112**: 351-361.
- Tsotsos J.K., (1989) "Knowledge Organization and Its Role in Representation and Interpretation for Time-Varying Data: The ALVEN System." in M. Fischler and O. Firschein, eds. *In Readings in Computer Vision*, Motgan Kaufmann, 498-514.
- Villarreal F.L., Waldman L.K., Lew W.Y.W., (1988) "A Technique for measuring regional two-dimensional finite strains in canine left ventricle," *Circ Res* **62**, 711-721.
- Waldman L.K., Fung Y.C., Covell J.W., (1985) "Transmural myocardial deformation in the canine left ventricle: Normal in vivo three-dimensional finite strains," *Circ Res*, **57**, 152-163.
- Young A., (1991) "Epicardial Deformation From Coronary Cineangiograms," in: L. Glass, P. Hunter, A. McCulloch, eds. *Theory of Heart: biomechanics, biophysics, and nonlinear dynamics of cardiac function*, New York, Springer-Verlag, 175-207.
- Young A.A., Hunter P.J., Smaill B.H., (1992) "Estimation of epicardial strain using the motions of coronary bifurcations in biplane cineangiography," *IEEE Trans Biomed Eng*, **39**, 526-531.
- Young A.A., Axel L., (1992) "Three-dimensional Motion and Deformation of the Heart Wall," *Radiology*, **185**, 241-247.
- Young A.A., Axel L., Dougherty L., Bogen D.K., Parenteau C.S., (1993) "Validation of Tagging with MR Imaging to Estimate Material Deformation," *Radiology*, **188**, 101-108.
- Young A.A., Kraitchman D.L., Axel L., (1994) "Deformable Models for Tagged MR Images: Reconstruction of Two- and Three-Dimensional Heart Wall Motion," Proceedings of IEEE Workshop on Biomedical Image Analysis, Seattle, WA, 317-323.
- Young A.A., Kramer C.M, Ferrari V.A., Axel L, Reichek N., (1994) "Three-Dimensional Left Ventricular Deformation in Hypertrophic Cardiomyopathy," *Circulation*, **90**(2), 854-867.
- Young A. A., Kraitchman D. L., Dougherty L., Axel L., (1995) "Tracking and finite element analysis of stripe deformation in magnetic resonance tagging," *IEEE Trans. on Medical Imaging*, **14**(3), 413-421.
- Zerhouni E.A., Parish D.M., Rogers W.J., Yang A., (1988) "Human heart: Tagging with MR imaging - a method for noninvasive assessment of myocardial motion," *Radiology*, **169**, 59-63.

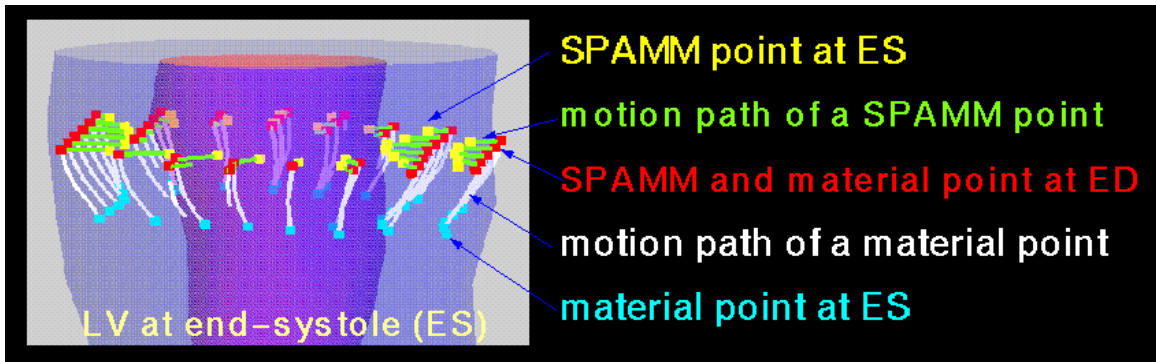


Figure 18: Material and SPAMM datapoint paths during systole.

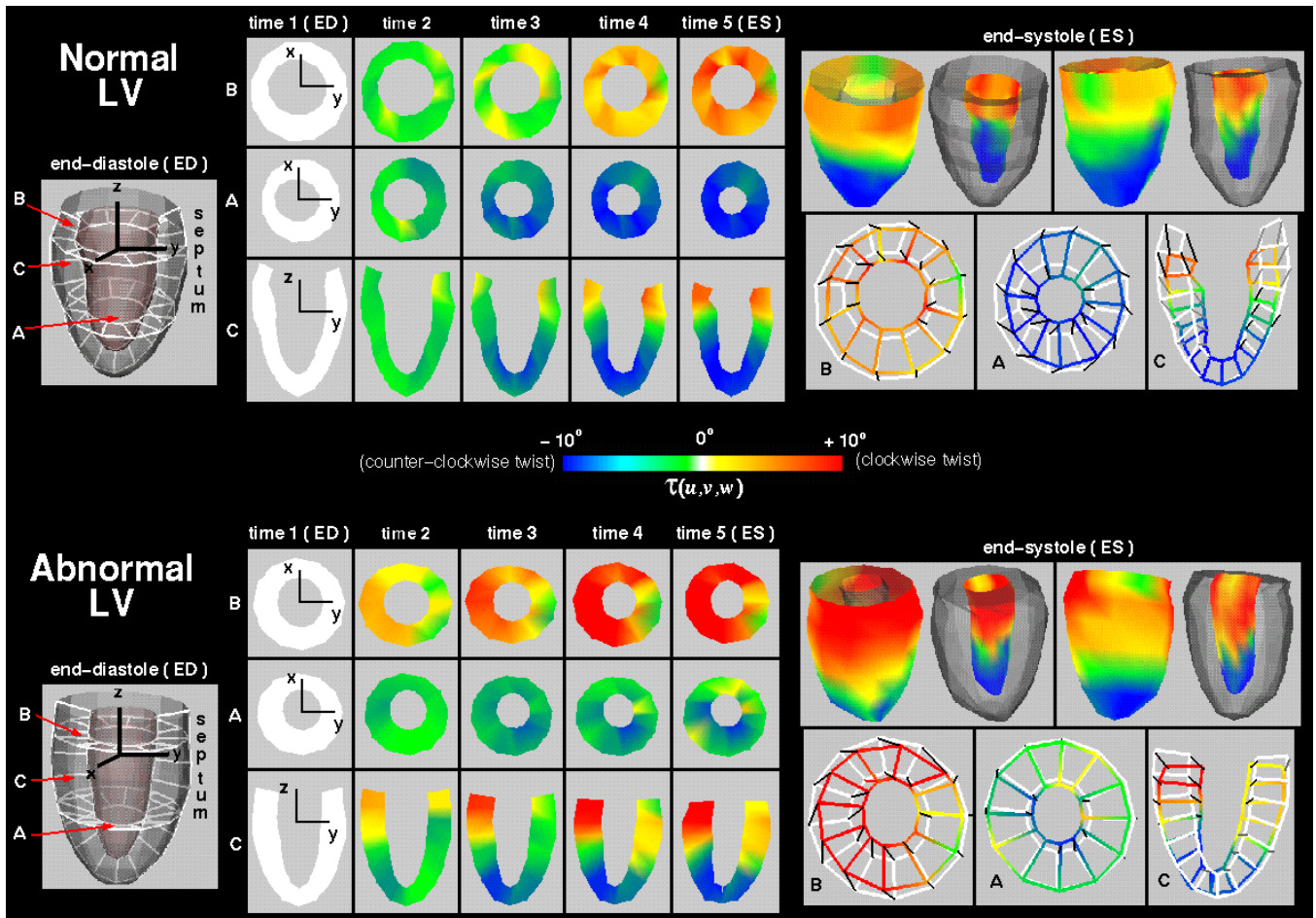


Figure 19: Quantitative visualization of the twisting parameter function for normal and abnormal LVs.